

# Exact classical dynamics of generic Lipkin-Meshkov-Glick model

Yu Dongyang<sup>1,2\*</sup>

<sup>1</sup>Department of Physics, Zhejiang University of Technology, No. 288, Liuhe Road, Hangzhou, 310023, Zhejiang, China.

<sup>2\*</sup>Zhejiang Provincial Key Laboratory and Collaborative Innovation Center for Quantum Precise Measurement, Zhejiang University of Technology, No. 288, Liuhe Road, Hangzhou, 310023, Zhejiang, China.

Corresponding author(s). E-mail(s): [dyyu21@zjut.edu.cn](mailto:dyyu21@zjut.edu.cn);

## Abstract

Lipkin-Meshkov-Glick (LMG) model is paradigmatic to study quantum phase transition in equilibrium or non-equilibrium systems and entanglement dynamics in a variety of disciplines. The generic LMG model usually incorporates two nonlinear interactions. The classical dynamics of the LMG model, in the thermodynamic limit where quantum fluctuations are negligible and with solely one nonlinear interaction, can be precisely represented using Jacobi elliptic functions, thereby providing a valuable benchmark for investigating quantum fluctuations in finite-size systems. In this work, we extend this analytical analysis into the regime where two nonlinear interactions are present, and successfully obtain the exact solutions of classical equations by constructing an auxiliary function that is a linear combination of the  $\mathbf{y}$  and  $\mathbf{z}$  component of the classical spin in the thermodynamic limit, and one-by-one map the classical dynamics into the complex plane of Jacobi elliptic functions. Based on these analytical solutions of the classical equations, we systematically investigate the dynamical phase transitions after a quench of nonlinear interactions, and analytically discuss the properties of dynamical phase transition triggered by the saddle points of isoenergetic surface. Our results can be measured and checked in a setup of Bose-Einstein condensates trapped in a homogeneous toroidal trap, and utilized to analyze dynamical phase transitions and entanglement dynamics of Lipkin-Meshkov-Glick model in presence of two nonlinear interactions.

**Keywords:** Lipkin-Meshkov-Glick model, classical dynamics, Jacobi elliptic function, dynamical phase transition, Bose-Einstein condensate

## 1 Introduction

Lipkin-Meshkov-Glick (LMG) model is firstly introduced in nuclear physics to describe  $N$  spins interacting with infinite-range interaction [1–3], also can be considered as a special limit of XY Heisenberg model in condensed matter physics [4]. Particularly in recent decades, LMG model has

already been engineered in various realistic platforms, i.e., a Bose-Einstein condensate (BEC) in a double well potential [5] or two-component/mode BECs [6], quantum gases in cavity QED [7, 8], thermal Bose gases [9] and superconducting circuits [10]. These experimental researches on LMG model make progress in its potential utilization in quantum information and precise

measurement [11]. Although the exact energy spectra of integrable LMG model has already been obtained [12] based on Bethe ansatz, large number of works are still being devoted into LMG and related models to figure out unexplored exotic phenomena, for instance, chaotic dynamics induced by nonequilibrium quantum fluctuations [13].

The Hamiltonian of a generic LMG model can be written down as follow,

$$\hat{H} = h\hat{J}_x + \frac{1}{N}(g_1\hat{J}_y^2 + g_2\hat{J}_z^2), \quad (1)$$

where the collective spin operators  $\hat{J}_\alpha = \sum_{j=1}^N \frac{1}{2}\sigma_j^\alpha$  ( $\alpha = x, y, z$ ) satisfying the SU(2) algebra,  $[\hat{J}_x, \hat{J}_y] = i\hat{J}_z$  ( $\hbar \equiv 1$  is set in this work),  $h$  is the magnetic field along  $x$  direction,  $g_{1,2}$  is the nonlinear interaction among spins align to  $y$  ( $z$ ) direction. Considerable attentions are paid to the largest angular momentum sector (the total angular momentum is conserved), specifically  $J = 2N$  to which the ground state belongs. In case of implementing LMG model in a setup of two-component/mode BECs [5, 6, 14, 15],  $\hat{J}_x = (\hat{a}^\dagger\hat{b} + \hat{b}^\dagger\hat{a})/2$ ,  $\hat{J}_y = (\hat{a}^\dagger\hat{b} - \hat{b}^\dagger\hat{a})/(2i)$ ,  $\hat{J}_z = (\hat{a}^\dagger\hat{a} - \hat{b}^\dagger\hat{b})/2$ .  $\hat{a}$  and  $\hat{b}$  represents the annihilation operator of Bosonic component (mode),  $[\hat{a}, \hat{a}^\dagger] = 1$  and  $[\hat{b}, \hat{b}^\dagger] = 1$ . Here it is worthy noting that we focus on the isolated dynamics of this generic LMG model, therefore its energy is also conserved. According to the value of nonlinear interactions, two scenarios can be classified, one is  $g_1g_2 = 0$  and the other is  $g_1g_2 \neq 0$ .

The first scenario only involving one nonlinear interaction, i.e.,  $g_1 = 0(g_2 \neq 0)$  or  $g_2 = 0(g_1 \neq 0)$  whenever Eq. (1) holds a  $Z_2$  symmetry, is widely utilized to generate spin-squeezing [16] and many-body entanglement [11, 17] by dynamics setup, where the one-tangle and concurrence can be estimated by the classical solutions [18, 19] that has already been obtained in terms of Jacobi elliptic function (JEF) [5]. Additionally, Eq. (1) in this scenario is also broadly used to study dynamical phase transition (DPT), a universal phenomenon that is triggered by a sudden quantum quench of control parameter [20] and quantified by nonequilibrium order parameters. Currently, Gaussian or semiclassical methods that can treat interactions

non-perturbatively in some limit (i.e.  $N \rightarrow \infty$ ) are the main approaches to deal with DPTs [13, 21].

Until now, however, the second scenario involving two nonlinear interactions, specifically  $g_1 \neq 0$  and  $g_2 \neq 0$  whenever Eq. (1) holds a  $Z_2 \times Z_2$  symmetry, has received little attentions. This lack of focus is largely due to the challenges in implementing this scenario in experimental setups, as it is significantly more difficult than the first scenario [6, 15]. While in terms of theoretical progress, to our best knowledge, the analytical solutions of classical dynamics of generic LMG model Eq. (1) in the thermodynamic limit are still lack so far [22], which prevents to investigate the LMG dynamics including its entanglement and DPT.

Here we extend the first scenario to the second scenario and successfully obtain analytical solutions of classical equations of Eq. (1) by constructing an auxiliary function [23] which still can be described by one member of JEFs the same as in the first scenario, and clearly show that the classical dynamics of generic LMG model can be one-by-one mapped not only into the Bloch sphere, but also into the complex plane of JEFs. The later mapping enables us, from a distinct perspective, to investigate semiclassical and quantum dynamics of LMG model. Based on this construction, we apply our analytical results to study the corresponding DPTs in the thermodynamic limit after a quench of nonlinear interactions. We give its generic dynamical phase diagram in terms of time-averaged order parameter and show that its DPTs are fully controlled by saddle points of isoenergetic surface. Furthermore, we ascertain that the dynamical criticality depends on the choice of time-averaged order parameter, which is absent in the first scenario. Finally we discuss the detection of DPTs in terms of BECs trapped in a homogeneous toroidal potential.

This article is arranged as follow. In Section 2, by introducing an auxiliary function  $X(t)$ , we derive the differential equation of  $X(t)$ , and give the corresponding analytical solutions according to the energy  $f_0$  and its corresponding extremums, and demonstrate the relation between asymptotic behaviors of classical dynamics and the landscape of energy. Then in Section 3, we apply our analytical results to discuss the corresponding DPTs after a quench and its detection. In Section 4, we give a conclusion.

## 2 Analytical solutions

Without loss of generality, the strength of magnetic field along  $x$  direction  $h \equiv 1$  is set, the Heisenberg equations of collective spin operators  $i\partial_t \hat{J}_j = [\hat{J}_j, \hat{H}]$ ,

$$\begin{aligned}\partial_t \hat{J}_x &= \frac{g_1 - g_2}{N} (\hat{J}_y \hat{J}_z + \hat{J}_z \hat{J}_y), \\ \partial_t \hat{J}_y &= -\hat{J}_z + \frac{g_2}{N} (\hat{J}_z \hat{J}_x + \hat{J}_x \hat{J}_z), \\ \partial_t \hat{J}_z &= \hat{J}_y - \frac{g_1}{N} (\hat{J}_y \hat{J}_x + \hat{J}_x \hat{J}_y).\end{aligned}\quad (2)$$

As  $N$  approaches infinity, the quantum fluctuations in LMG model eventually diminish to zero, which can be understood by intuitively introducing the 'renormalized' operators,  $2\hat{J}_{x,y,z}/N$ ,

$$\left[\frac{2\hat{J}_x}{N}, \frac{2\hat{J}_y}{N}\right] = i\hbar_{\text{eff}} \frac{2\hat{J}_z}{N} \quad (3)$$

with an effective Plank's constant  $\hbar_{\text{eff}} = 2/N$ . Therefore,  $\hbar_{\text{eff}} \rightarrow 0$  in the thermodynamic limit, and the spin is classical. Let  $S_j = 2\langle\Psi_0|\hat{J}_j(t)|\Psi_0\rangle/N$  where the initial state  $|\Psi_0\rangle$  is a spin coherent state,

$$\begin{aligned}\partial_t S_x &= (g_1 - g_2) S_y S_z, \\ \partial_t S_y &= (-1 + g_2 S_x) S_z, \\ \partial_t S_z &= (1 - g_1 S_x) S_y.\end{aligned}\quad (4)$$

constrained by the total angular momentum  $S_x^2 + S_y^2 + S_z^2 = 1$ . Additionally, Eqs. (4) are also imposed to evolve on the isoenergetic surface with energy  $f_0 = 2\langle\Psi_0|\hat{H}|\Psi_0\rangle/N$  because we only consider an isolated system.

Before discussing the generic classical dynamics of Eq. (1), let us briefly review the classical solutions already known. When  $g_1 = g_2 = g$ ,  $S_x$  is also a constant, a  $U(1)$  symmetry emerges,

$$\begin{aligned}\partial_t^2 S_y &= -(1 - g S_x)^2 S_y, \\ \partial_t^2 S_z &= -(1 - g S_x)^2 S_z,\end{aligned}\quad (5)$$

satisfying  $f_0 = S_x + \frac{g}{2}(1 - S_x^2)$ . The solution can be written down as follow,  $S_x = (1 - \sqrt{D})/g$  ( $S_x = f_0$  when  $g = 0$ ),

$$S_y(t) = A \sin(\sqrt{D}t + \psi),$$

$$S_z(t) = -A \cos(\sqrt{D}t + \psi), \quad (6)$$

with  $A = 2\sqrt{(\sqrt{D} + f_0 g - 1)/g^2}$ ,  $D = g^2 - 2f_0 g + 1$ , the phase  $\psi$  is determined by the initial condition.

In the first scenario (here we only consider the case  $g_1 = 0$  and  $g_2 \neq 0$ ), Eq. (4) can be transformed into a first-order nonlinear differential equation,

$$1 - f_0^2 = (\partial_t S_z)^2 + (1 - g_2 f_0) S_z^2 + \frac{g_2^2}{4} S_z^4. \quad (7)$$

The left-hand-side of Eq. (7) can be understood as a linear combination between the square of energy and total angular momentum. While the right hand of Eq. (7) actually means that a classical particle moves in a double well potential,  $V(S_z) = ((1 - g_2 f_0) S_z^2 + g_2^2 S_z^4/4)/2$ . Hence, the differential equation of  $S_z$  is identical to one member of JEFs after a simple transformation as discussed in next section. Therefore, the analytical solution of Eq. (7) is obtained accordingly [5, 6, 18].

Nonetheless, attempts to construct the analytical solutions in the second scenario rarely success until recently. In fact, the energy can be written down as follow,

$$f_0 = S_x + \frac{1}{2}(g_1 S_y^2 + g_2 S_z^2). \quad (8)$$

Suppose that  $\{S_x, S_y, S_z\}$  is the solution of Eq. (4) at a given parameter set  $\{g_1, g_2, f_0\}$ , then  $\{-S_x, S_y, S_z\}$  is also the solution at  $\{-g_1, -g_2, -f_0\}$ . What is more, we observe that the solution is invariant under the transformation  $S_{y,z} \rightarrow S_{z,y}$ ,  $g_{1,2} \rightarrow g_{2,1}$  and  $t \rightarrow -t$  because of time-reversal-like symmetry. Therefore, for clarity, *in this section we will only solve Eq. (4) in case of  $f_0 \geq 0$  and i.e.,  $g_1 \geq g_2$  unless specified*. While the solutions in the remained regimes can be obtained according to the aforementioned transformations.

The initial values of  $S_{x,y,z}(t=0)$  are parameterized by  $\theta_0$  and  $\phi_0$ ,  $S_z(0) = \cos(\theta_0)$ ,  $S_x(0) = \sin(\theta_0) \cos(\phi_0)$ ,  $S_y(0) = \sin(\theta_0) \sin(\phi_0)$  with  $\theta_0 \in [0, \pi]$  and  $\phi_0 \in [0, 2\pi]$ , then,

$$f_0 = \sin \theta_0 \cos \phi_0 + \frac{g_1}{2} \sin^2 \theta_0 \sin^2 \phi_0 + \frac{g_2}{2} \cos^2 \theta_0. \quad (9)$$

The classical dynamics Eq. (4) is greatly affected by the landscape of  $f_0$ , i.e., the minimum, saddle-point and maximum [24], which are determined by  $\partial_{\theta_0} f_0 = 0$  and  $\partial_{\phi_0} f_0 = 0$ ,

$$\begin{aligned}\cos \theta_0 (\cos \phi_0 + \sin \theta_0 (g_1 \sin^2 \phi_0 - g_2)) &= 0, \\ \sin \theta_0 \sin \phi_0 (-1 + g_1 \sin \theta_0 \cos \phi_0) &= 0.\end{aligned}\quad (10)$$

In general, for any real values of  $g_1$  and  $g_2$ , six trivial solutions of Eq. (10) always exist, the first and second solution is  $(\theta_0 = \pi/2, \phi_0 = 0)$  and  $(\theta_0 = \pi/2, \phi_0 = \pi)$ , corresponding to  $f_0 = 1$  and  $f_0 = -1$  respectively. While the rest four solutions  $(\theta_0 = 0 \text{ or } \pi, \phi_0 = \pi/2 \text{ or } 3\pi/2)$  share the same energy  $f_0 = g_2/2$ . We note that the classical energy surface obtained here coincides with the one based on spin-coherent state [25, 26].

An analysis on the landscape of  $f_0$  when  $|g_1| \geq 1$  or  $|g_2| \geq 1$  shows that two additional saddle points emerge (see Appendix: C). Importantly, we discover that the position of each of these saddle points depends solely on one interaction parameter, either  $g_1$  or  $g_2$ , rather than both simultaneously. This feature makes that the classical temporal evolution of  $\langle \hat{J}_y \rangle$  and  $\langle \hat{J}_z \rangle$  looks like independent. As a consequence, it is possible for us to construct an auxiliary function that represents the classical dynamics of Eq. (4) by a single variable, as discussed below.

Firstly, defining an auxiliary function  $X(t) = a_1 S_y(t) + a_2 S_z(t)$  with  $a_1^2 = g_1(g_1 - g_2)/(g_1^2 + g_2^2)$  and  $a_2^2 = g_2(g_2 - g_1)/(g_1^2 + g_2^2)$ , we find that the classical dynamics of  $X$  can be written down in a simple formula,

$$\partial_t^2 X + DX + \frac{g_1^2 + g_2^2}{2} X^3 = 0, \quad (11)$$

with an effective frequency  $D$ ,

$$D = 1 + g_1 g_2 - f_0 (g_1 + g_2). \quad (12)$$

Then, Eq. (11) could be further simplified as a first-order ordinary nonlinear differential equation constrained by the conservation of angular momentum and energy  $f_0$ ,

$$(\partial_t X)^2 + DX^2 + \frac{g_1^2 + g_2^2}{4} X^4 = (1 - f_0^2) \frac{(g_1 - g_2)^2}{g_1^2 + g_2^2}, \quad (13)$$

The first scenario can be considered as a special case of the second scenario because when  $g_1 = 0$  and  $g_2 \neq 0$ ,  $a_1 = 0$  and  $a_2 = 1$ ,  $X = S_z$ . As a result, Eq. (13) returns to Eq. (7). When  $g_1 \neq 0$  and  $g_2 = 0$ ,  $a_1 = 1$  and  $a_2 = 0$ ,  $X = S_y$  has a similar formula. While for the second scenario, we argue that our generalization to the second scenario lies on a fact that the position of each of emergent saddle points when  $|g_1| > 1$  and  $|g_2| > 1$  depends solely on one nonlinear interaction, either  $g_1$  or  $g_2$ , rather both of them. When  $X \in \mathcal{R}$ , i.e.  $g_2 < 0 < g_1$ , Eq. (11) is a special case of Duffing's equation with no damping and driving force, and considered as an analytic continuation of Duffing's equation into the complex plane when  $X \in \mathcal{C}$ , i.e.,  $g_1 > g_2 > 0$  (please see the discussions in Appendix: A). Nonetheless, this is quite different from the previous works, where  $X$  is defined in real axis [27] or the cubical term is like  $|X|^2 X$  [23]. In a word, the dynamics of  $X$  is identical to a classical particle that is governed by a complex double well potential,  $V(X) = (DX^2 + (g_1^2 + g_2^2)X^4)/2$  with  $X \in \mathcal{C}$ . We note here that strictly speaking, Eq. (11) (13) can not be applied to the case  $g_1 = g_2$ , because  $a_1 = a_2 = 0$ .

By introducing

$$\tau = \frac{\sqrt{g_1^2 + g_2^2}}{2} t, \quad (14)$$

we recast Eq. (13) into a more compact form,

$$(\partial_\tau X)^2 = P[X] \equiv -(X^4 + uX^2 + v), \quad (15)$$

with

$$\begin{aligned}u &= \frac{4D}{g_1^2 + g_2^2}, \\ v &= 4(f_0^2 - 1) \frac{(g_1 - g_2)^2}{(g_1^2 + g_2^2)^2}.\end{aligned}\quad (16)$$

Basically, the analytical solutions of Eq. (15) can be classified into four regimes and expressed as one member of the family of JEFs shown in Table. 1. This classification is based on the sign of  $v$ ,  $u$  and the discriminant  $\Delta$  of  $P[X] = 0$ ,

$$\Delta = \frac{4R_1 R_2}{(g_1^2 + g_2^2)^2}, \quad (17)$$

with

$$R_{1,2} = g_{1,2}^2 - 2f_0g_{1,2} + 1. \quad (18)$$

In fact, the critical points set by  $\Delta = 0$  correspond to the minimum/maximum/saddle points of  $f_0$  in parameter space, or equivalently, the critical parameters of  $g_{1,2}$  are given as  $g_{\pm}(f_0)$  for a fixed value of  $f_0$ ,

$$g_{\pm}(f_0) = f_0 \pm \sqrt{f_0^2 - 1} \text{ as } |f_0| \geq 1. \quad (19)$$

For clarity, we take  $f_0 = 1.6$  as an example to display the **Reg. II** (Sec. 2.2.1), **Reg. III** (Sec. 2.2.2), and **Reg. IV** (Sec. 2.2.3) in Fig. 1 (where we do not explicitly depict the **Reg. I** (Sec. 2.1), because **Reg. I** covers the entire  $g_1 - g_2$  plane when  $0 \leq f_0 \leq 1$ ). In each regime, Eq. (15) can be ultimately transformed into the differential equation of a member within the set of JEFs as shown in Eq. (21), (30), (39), and (50). Then the analytical solutions of Eq. (15) can be explicitly expressed in terms of JEFs.

To fully determine  $X(t)$ , however, two initial conditions of  $X$  are further needed,  $X(0) = a_1S_y(0) + a_2S_z(0)$  and its first order derivative with respect to time  $X'(0) = a_1S'_y(0) + a_2S'_z(0)$  (given by Eq. (4)). After  $X(t)$  of Eq. (15) obtained, the analytical solution  $S_{x,y,z}$  can be constructed according to the sign of  $a_{1,2}$  (see Appendix A) and compared with the numerical ones of Eq. (4), which shows an excellent consistency with each other, see Fig. (2, 3, 4, 5). It is worthy noting that the high-precision numerical solutions of Eq. (4) can be easily obtained in a laptop computer with few cores.

## 2.1 Reg. I: $0 \leq f_0 \leq 1$

The solution of Eq. (15) is unique when  $0 \leq f_0 \leq 1$ . By introducing  $Y = X\sqrt{w_-^2 + w_+^2}/(w_-w_+)$ ,  $\tau' = \sqrt{w_-^2 + w_+^2}\tau$  (Eq. (14)), and  $w_{\pm} = \sqrt{\sqrt{\Delta} \pm u}/2$ , Eq. (15) is recast as follow (see Appendix B),

$$(\partial_{\tau'}Y)^2 = (1 - m'Y^2)(1 + mY^2), \quad (20)$$

with Jacobi elliptic modulus (JEM)  $m = w_-^2/(w_-^2 + w_+^2)$ . Actually, Eq. (20) is identical to

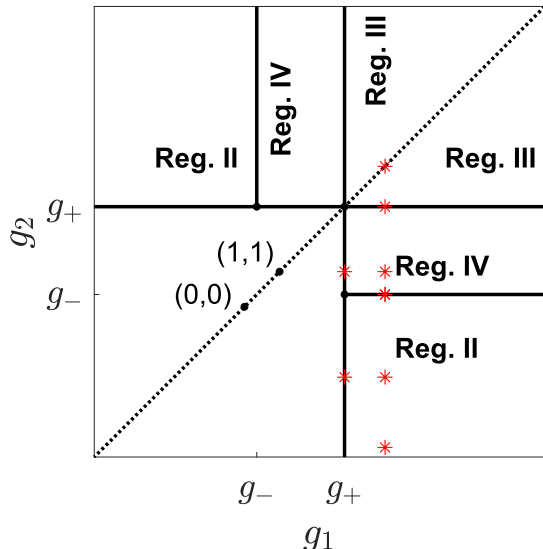


**Fig. 1:** (color online) Solutions of Eq. (15) can be classified into four regimes in parameter space. **Reg. I** (Sec. 2.1) always exists in the whole  $g_1 - g_2$  plane when  $0 \leq f_0 \leq 1$ , while the regimes of **Reg. II** (Sec. 2.2.1), **Reg. III** (Sec. 2.2.2) and **Reg. IV** (Sec. 2.2.3) are shown as  $f_0 = 1.6$ . Typical points (red asterisks) are chosen as examples to demonstrate the classical dynamics and especially show the consistency between analytical (Eq. (15)) and numerical (Eq. (4)) solutions, see Fig. (2, 3, 4, 5). Here the  $g_1 = g_2$  line is particularly plotted (dotted line) as a guide line.

the differential equation of JEF  $\text{sd}(z, m)$  [28]. As a consequence, the solution of Eq. (15) is obtained,

$$X(t) = \frac{w_-w_+}{\sqrt{w_-^2 + w_+^2}} \text{sd}(\xi\sqrt{w_-^2 + w_+^2}\tau + p_0, m), \quad (21)$$

here the parameters  $p_0$  and  $\xi = \pm 1$  are determined by the initial values  $X(t = 0)$ ,

$$X(0) = w_-w_+/\sqrt{w_-^2 + w_+^2} \cdot \text{sd}(p_0, m), \quad (22)$$

$$X'(0) \propto \xi \cdot \text{cd}(p_0, m) \cdot \text{nd}(p_0, m). \quad (23)$$

Because both  $\text{cd}(z, m)$  and  $\text{nd}(z, m)$  are even functions of  $z$ , therefore, the temporal evolution frequency  $\Omega$  of periodical solution Eq. (15),

$$\Omega = \frac{\pi}{2\sqrt{2}K} (R_1R_2)^{\frac{1}{4}}, \quad (24)$$

	Range of $f_0$	Ranges of $g_1$ and $g_2$	$v$	$u$	$\Delta$	JEF
<b>Reg. I</b> (Sec. 2.1)	$0 \leq f_0 \leq 1$	the whole range	-			sd(z,m) (Eq. (21))
<b>Reg. II</b> (Sec. 2.2.1)	$f_0 \geq 1$	$g_2 \leq g_-(f_0),$ $g_+(f_0) \leq g_1$		-		nd(z,m) (Eq. (30))
<b>Reg. III</b> (Sec. 2.2.2)		$g_+(f_0) \leq g_2 \leq g_1$		+		sn(z,m) (Eq. (39))
<b>Reg. IV</b> (Sec. 2.2.3)		$g_-(f_0) \leq g_2 \leq g_+(f_0)$			-	

**Table 1:** Four distinct regimes (Reg. I-IV) of Eq. (15) are identified based on the signs of  $v$ ,  $u$  and  $\Delta$ , with clear parameter ranges for each regime detailed. The blanks in the fifth column indicate indeterminate signs of  $u$ . The last column shows the corresponding JEF for each regime.

with the complete elliptic integral of the first kind

$$K(m) = \int_0^{\pi/2} d\varphi (1 - m \sin^2(\varphi))^{-1/2}. \quad (25)$$

The definition of  $K(m)$  is the same throughout this work.

When  $|g_1| \ll 1$  and  $|g_2| \ll 1$ , the cubic term  $X^3$  is negligible. Hence, a Rabi oscillation is observed because of the dominated linear term (15), see Fig. (2)(a). In general, the temporal evolution of  $X$  or  $S_{x,y,z}$  depends significantly on the JEM,

$$m = \frac{1}{2} \left( 1 - \text{Sgn}(D) \sqrt{1 - \frac{(g_1 - g_2)^2 (1 - f_0^2)}{R_1 R_2}} \right), \quad (26)$$

here  $\text{Sgn}(\cdot)$  means a sign function. In case that  $g_1$  approaches to  $g_2$  ( $g_1 \rightarrow g$  and  $g_2 \rightarrow g$ , the JEM  $m \rightarrow 0$ ), the dynamics of  $S_{x,y,z}$  oscillates sinusoidally with frequency  $\Omega \rightarrow \sqrt{g^2 - 2f_0g + 1}$ , consistent with the results of Eq. (6), see Fig. (2)(b).

While as  $f_0 \rightarrow 1$ , a simple expression of JEM is obtained,

$$m \Big|_{f_0 \rightarrow 1} = \frac{1}{2} (1 - \text{Sgn}(1 - g_1) \cdot \text{Sgn}(1 - g_2)), \quad (27)$$

In case  $g_1 > 1$  and  $g_2 > 1$  (or  $g_1 < 1$  and  $g_2 < 1$ ), the JEM  $m \rightarrow 0$  when  $f_0 \rightarrow 1$ , which means an exact Rabi oscillation with  $\Omega \rightarrow \sqrt{(g_1 - 1)(g_2 - 1)}$  even though the nonlinear interactions, i.e.  $g_1$  and  $g_2$ , may be very strong (see

Fig. 2(c)). While  $g_1 > 1$  and  $g_2 < 1$  (or  $g_1 < 1$  and  $g_2 > 1$ ),  $m \rightarrow 1$ ,  $X(t) \propto \sinh(\sqrt{w_-^2 + w_+^2} \tau + p_0)$ . Therefore, around the initial time, the dynamics of  $S_{x,y,z}$ , no matter what the strength of  $|g_1|$  and  $|g_2|$  is, undergoes an exponential growth and saturates around the saddle point of  $f_0$  ( $(S_x, S_y, S_z) \approx (1, 0, 0)$ ) with vanishing frequency  $\Omega \rightarrow 0$ , as depicted in Fig. (2(d)).

## 2.2 $f_0 \geq 1$

For a fixed  $f_0 \geq 1$ , although  $v \geq 0$  always holds on (see Table. 1), the solutions of Eq. (15) still depend on the signs of  $\Delta$  and  $u$  which will change as varying  $g_2$ , see Table 1 and Fig. 1. In general, three regimes are classified further: **Reg. II** (Sec. 2.2.1) where  $g_2 \leq g_-(f_0)$ ,  $\Delta \geq 0$ , and  $u \leq 0$ ; **Reg. III** (Sec. 2.2.2) where  $g_2 \geq g_+(f_0)$ ,  $\Delta \geq 0$  and  $u \geq 0$ ; **Reg. IV** (Sec. 2.2.3) where  $g_-(f_0) < g_2 < g_+(f_0)$ ,  $\Delta \leq 0$ . Next we will discuss them individually.

### 2.2.1 Reg. II: $g_2 \leq g_-(f_0)$ and $g_+(f_0) \leq g_1$

In this case,  $\Delta > 0$ ,  $u < 0$ , and  $\sqrt{u^2/4 - v} < |u|/2 = -u/2$ . By defining  $Y = X/w_-$ ,  $\tau' = w_+ \tau$  (Eq. (14)),  $w_{\pm} = \sqrt{-u/2 \pm \sqrt{\Delta}}$  and the corresponding JEM  $m = 1 - w_-^2/w_+^2$ ,

$$m = \frac{2\sqrt{R_1 R_2}}{\sqrt{R_1 R_2} - D}, \quad (28)$$



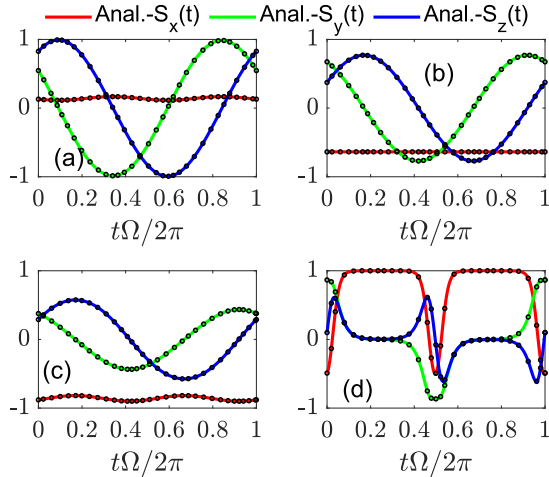


**Fig. 2:** (color online) Comparisons between the analytical solutions Eq. (21) and the numerical ones Eq. (4). The solid red, green and blue line corresponds to the  $S_x(t)$ ,  $S_y(t)$  and  $S_z(t)$ , respectively. While the black circles are the corresponding results obtained by numerically solving Eq. (4). For subplot (a-d), (a)  $g_1 = 0.5$ ,  $g_2 = 0.6$ , and  $f_0 = 0.38$ ; (b),  $g_1 = 4$ ,  $g_2 = 4 - \epsilon$ , and  $f_0 = 0.59$ ; (c),  $g_1 = 20$ ,  $g_2 = 11$ , and  $f_0 = 1 - \epsilon$ ; (d),  $g_1 = 4$ ,  $g_2 = -2$ , and  $f_0 = 1 - \epsilon$ . Here  $\epsilon$  is an infinitesimal positive real number.

we find that Eq. (15) can be rewritten down as (Appendix (A))

$$(\partial_{\tau'} Y)^2 = (Y^2 - 1)(1 - (1 - m)Y^2), \quad (29)$$

which is identical to the differential equation of  $\text{nd}(z, m)$  [28]. Therefore, the analytical solutions of Eq. (15)

$$X(t) = w_- \cdot \text{nd}(\xi w_+ \tau + p_0, m), \quad (30)$$

here  $p_0$  and  $\xi = \pm 1$  satisfying

$$X(0) = w_- \cdot \text{nd}(p_0, m) \quad (31)$$

$$X'(0) \propto \xi \frac{\text{cn}(p_0, m) \cdot \text{sn}(p_0, m)}{\text{dn}^2(p_0, m)}. \quad (32)$$

And the frequency  $\Omega$ ,

$$\Omega = \frac{\pi}{2\sqrt{2}K} \sqrt{\sqrt{R_1 R_2} + D}. \quad (33)$$

Let us examine what feature of Eq. (15) is when  $g_1 \rightarrow g_+(f_0)$  or  $g_2 \rightarrow g_-(f_0)$ . In this case, the JEM  $m \rightarrow 0$ . Therefore, the dynamics becomes completely a sinusoidal function with finite frequency

$$\lim_{g_1 \rightarrow g_+} \Omega = (f_0^2 - 1)^{\frac{1}{4}} \sqrt{2(g_+(f_0) - g_2)}, \quad (34)$$

$$\lim_{g_2 \rightarrow g_-} \Omega = (f_0^2 - 1)^{\frac{1}{4}} \sqrt{2(g_1 - g_-(f_0))}, \quad (35)$$

as depicted in Fig. 3(a-b). It is worthy noting that as  $g_1 \rightarrow g_+(f_0)$  or equivalently  $f_0 \rightarrow (g_1 + 1/g_1)/2$ , the classical spin is slightly shaking around the maximum of  $f_0$  as time goes on, see Fig. (3)(a).

As in **Reg. I** (2.1), the JEM  $m \rightarrow 1$  when  $f_0 \rightarrow 1$ , similar exponential growth of classical dynamics occurs, see Fig. (2)(d) and Fig. (3)(c). However, distinct feature still needs to be emphasized around the saddle point  $f_0 = 1$  ( $\theta_0 = \pi/2$  and  $\phi_0 = 0$ , see Appendix C). Although  $\Omega \rightarrow 0$  when  $f_0 \rightarrow 1$ , we find that the frequency  $\Omega$  suffers from a discontinuity as  $f_0$  crossing  $f_0 = 1$ . For instance,  $\Omega(4, -2, 1 - 10^{-6}) \approx 0.521$  and  $\Omega(4, -2, 1 + 10^{-6}) \approx 1.042$ . This discontinuity becomes more clear if we calculate the limit,

$$\lim_{\epsilon \rightarrow 0^+} \frac{\Omega(g_1, g_2, 1 - \epsilon)}{\Omega(g_1, g_2, 1 + \epsilon)} = \frac{1}{2}, \quad (36)$$

which corresponds to the sharp change of trajectory topology because two fixed points emerge. This phenomenon is also termed as DPT already observed in experiment [8, 10]. At last, it would be easily proven that whatever value of  $f_0$  ( $f_0 > 1$ ) is, the JEM  $m \rightarrow 1$  when both nonlinear interaction  $g_1$  and  $g_2$  are strong enough ( $g_1 \rightarrow +\infty$  and  $g_2 \rightarrow -\infty$ ). As expected, an exponential divergence of classical dynamics occurs with vanishing  $\Omega$  whatever the initial state is (Fig. (3)(d)).

### 2.2.2 Reg. III: $g_+(f_0) \leq g_2 \leq g_1$

As shown in Table. 1,  $\Delta \geq 0$  and  $u \geq 0$  and  $\sqrt{u^2/4 - v} < |u|/2 = u/2$  in this regime. By introducing  $\tau' = i\xi w_+ \tau$  (Eq. (14), and  $\xi = \pm 1$  determined by the initial conditions),  $w_{\pm} = \sqrt{u/2 \pm \sqrt{\Delta}}$ ,  $Y = X/w_-$  and the JEM  $m = w_-^2/w_+^2$ ,

$$m = \frac{D - \sqrt{R_1 R_2}}{D + \sqrt{R_1 R_2}}, \quad (37)$$

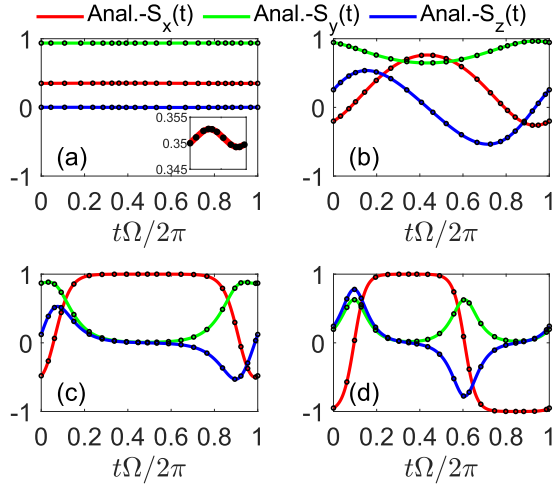


**Fig. 3:** (color online) Comparisons between the analytical solutions Eq. (30) and the numerical ones Eq. (4). The solid red, green and blue line corresponds to the  $S_x(t)$ ,  $S_y(t)$  and  $S_z(t)$ , respectively. While the black circles are the corresponding results obtained by numerically solving Eq. (4). For subplot (a-d), (a),  $g_1 = g_+(f_0) + \epsilon$ ,  $g_2 = -2$ , and  $f_0 = 1.6$ ; (b),  $g_1 = 4$ ,  $g_2 = g_-(f_0) + \epsilon$ , and  $f_0 = 1.6$ ; (c),  $g_1 = 4$ ,  $g_2 = -4$ , and  $f_0 = 1 + \epsilon$ ; (d)  $g_1 = 20000$ ,  $g_2 = -13000$ , and  $f_0 = 4.5$ , here  $\epsilon$  is an infinitesimal positive real number. An inset in Fig. 3(a) shows the slightly shaking of  $S_x(t)$  at a closer scale.

we discover that Eq. (15) can be rewritten as follow,

$$(\partial_{\tau'} Y)^2 = (1 + Y^2)(1 + mY^2), \quad (38)$$

which is identical to the differential equation of  $\text{sc}(z, m)$  [28]. Therefore the solution of Eq. (15)

$$X(t) = iw_- \cdot \text{sn}(\xi w_+ \tau + p_0, m), \quad (39)$$

here the imaginary transformation of JEFs,  $i \cdot \text{sn}(u, m) = \text{sc}(iu, 1 - m)$  has been applied. Similar to the previous cases,  $p_0$  and  $\xi$  are determined by the initial conditions,

$$X(0) = iw_- \cdot \text{sn}(p_0, m), \quad (40)$$

$$X'(0) \propto i\xi \text{cn}(p_0, m) \cdot \text{dn}(p_0, m). \quad (41)$$

The temporal evolution of  $X(t)$  can be viewed as a trajectory that parallels to the real axis in complex

plane because  $p_0 \in \mathcal{C}$  with the frequency

$$\Omega(g_1, g_2, f_0) = \frac{\pi}{2\sqrt{2}K} \sqrt{\sqrt{R_1 R_2} + D}. \quad (42)$$

As  $g_1$  approaches to  $g_2$  ( $g_1 \rightarrow g$  and  $g_2 \rightarrow g$ ), the JEM  $m \rightarrow 0$ , the dynamics behave the same as in **Reg. I** (Sec. 2.1) with frequency  $\Omega \rightarrow \sqrt{g^2 - 2f_0g + 1}$  (Fig. 2(b) and Fig. 4(a)). In contrast to the behavior around the saddle-point  $f_0 = 1$  in **Reg. II** (Sec. 2.2.1), however, we find the frequency  $\Omega$  is continuous around the saddle point  $f_0 = (g_2 + 1/g_2)/2$ ,

$$\lim_{\epsilon \rightarrow 0^+} \Omega(g_1, g_+ + \epsilon, f_0) = \lim_{\epsilon \rightarrow 0^+} \Omega(g_1, g_+ - \epsilon, f_0) = 0. \quad (43)$$

This continuity means that as  $g_2$  crossing  $g_+(f_0)$ , three different trajectories, i.e., see Fig. 4(b,c) and Fig. 5(b) (that will be discussed in next subsection), approximately share the same frequency because all of them envelop even number of saddle-points. Further investigation is needed to uncover the corresponding properties of these three distinct trajectories in relation to coherent atomic oscillations [5].

Furthermore, because  $f_0 = 1$  in current **Reg. III** (Sec. 2.2.2) is a local minimum (Fig. (C2)(g)), a similar frequency continuity still holds around  $f_0 = 1$ ,

$$\begin{aligned} \lim_{f_0 \rightarrow 1^+} \Omega(g_1, g_2, f_0) &= \lim_{f_0 \rightarrow 1^-} \Omega(g_1, g_2, f_0) \\ &= \sqrt{(g_1 - 1)(g_2 - 1)}, \end{aligned} \quad (44)$$

which corresponds to distinct trajectories on the surface of Bloch sphere, respectively. In relation to a BEC realization, the former trajectory around Eq. (44) is the plasma oscillation around  $(S_x, S_y, S_z) = (1, 0, 0)$ , while the later is the  $\pi$ -phase oscillation around  $(S_x, S_y, S_z) = (-1, 0, 0)$ , please see Fig. 2(c) and Fig. 4(d).

### 2.2.3 Reg. IV: $g_-(f_0) \leq g_2 \leq g_+(f_0)$

By introducing  $t_- = -u/2 + \sqrt{v}$ ,  $w_{\pm} = (1 \pm \sqrt{t_-}/(2\sqrt{v}))/2$ ,  $Y = \sqrt{w_+}(X - v^{\frac{1}{4}})/(\sqrt{w_-}(X + v^{\frac{1}{4}}))$ ,  $\tau' = 2i\xi v^{1/4} w_+ \tau$  (Eq. (14)),



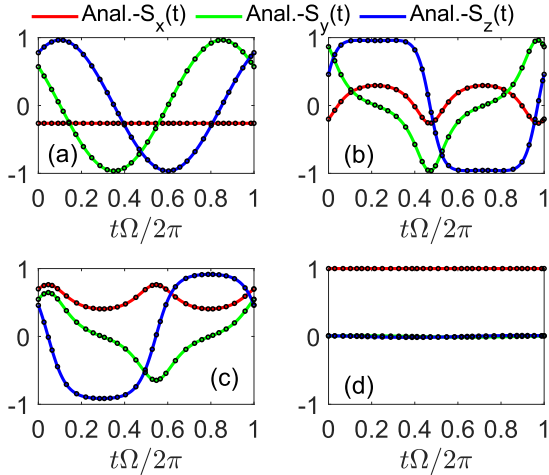


**Fig. 4:** (color online) Comparisons between the analytical solutions Eq. (39) and the numerical ones Eq. (4). The solid red, green and blue line corresponds to the  $S_x(t)$ ,  $S_y(t)$  and  $S_z(t)$ , respectively. While the black circles are the corresponding results obtained by numerically solving Eq. (4). For subplot (a-d), (a)  $g_1 = 4$ ,  $g_2 = 4 - \epsilon$ , and  $f_0 = 1.6$ ; (b-c),  $g_1 = 4$ ,  $g_2 = g_+(f_0) + \epsilon$ , and  $f_0 = 1.6$  (with different initial states); (d),  $g_1 = 20$ ,  $g_2 = 11$ , and  $f_0 = 1 + \epsilon$ . Here  $\epsilon$  is an infinitesimal positive real number.

and the JEM  $m = (w_-/w_+)^2$ ,

$$m = \left( \frac{1 - \sqrt{\frac{1}{2} \left( 1 - \frac{D}{(g_1 - g_2)\sqrt{f_0^2 - 1}} \right)}}}{1 + \sqrt{\frac{1}{2} \left( 1 - \frac{D}{(g_1 - g_2)\sqrt{f_0^2 - 1}} \right)}} \right)^2, \quad (45)$$

we find that the differential equation of  $Y$  can be recast as follow,

$$(\partial_\tau Y)^2 = (Y^2 + 1)((1 - m)Y^2 + 1), \quad (46)$$

which is identical to the differential equation of JEF  $sz(z, m)$ . Hence, the analytical formula of  $Y(t)$  can be expressed as follow,

$$Y(t) = i\sqrt{\frac{w_-}{w_+}} \cdot \text{sn}(2\xi v^{\frac{1}{4}} b_+ \tau + p_0, m), \quad (47)$$

where  $p_0 \in \mathcal{C}$  and  $\xi = \pm 1$  are determined by the initial conditions,

$$Y(0) = \frac{X(0) - \alpha}{X(0) + \alpha} = i\sqrt{\frac{w_-}{w_+}} \cdot \text{sn}(p_0, m), \quad (48)$$

and

$$\left. \frac{\partial Y(t)}{\partial t} \right|_{t=0} \propto i\xi \cdot \text{cn}(p_0, m) \cdot \text{dn}(p_0, m). \quad (49)$$

Finally, the analytical solution of  $X(t)$  is obtained

$$X(t) = v^{\frac{1}{4}} \frac{1 + Y(t)}{1 - Y(t)}, \quad (50)$$

with frequency,

$$\Omega = \frac{\pi}{4K} \left( \sqrt{2} \sqrt{\sqrt{f_0^2 - 1} \cdot |g_1 - g_2|} + \sqrt{\sqrt{f_0^2 - 1} \cdot |g_1 - g_2| - D} \right). \quad (51)$$

Because frequency is continuous around the boundary  $g_2 = g_\pm(f_0)$  as already discussed in **Reg. II** (Sec. 2.2.1) and **Reg. III** (Sec. 2.2.2). Here we just present the corresponding temporal evolution of  $S_{x,y,z}(t)$ , see Fig. (5)(a,b). A note is that Fig. (5)(b) corresponds to the third trajectory sharing the same frequency as discussed in Eq. (43). In case  $f_0 > 1$ , the corresponding frequency is the same formula as in Eq. (34) when  $g_1 \rightarrow g_+(f_0)$ . And a similar sinusoidal oscillation around  $f_0 = (g_1 + 1/g_1)/2$  is present in Fig. (5)(c).

### 3 Dynamical phase transitions

LMG model is widely used to investigate DPT after a quench of controlling parameters [20, 29]. However, due to the limit of experimental setups, these discussions are much more focused on the first scenario rather than the second one, both of which would be engineered in the hybrid of cavity-cold atomic gases [30, 31] or BEC in a toroidal trap [15]. In this section, we apply our analytical results to uncover the properties of DPT in the thermodynamic limit especially for the second scenario and discuss the detection of DPTs in the setup of BECs in a toroidal trap.

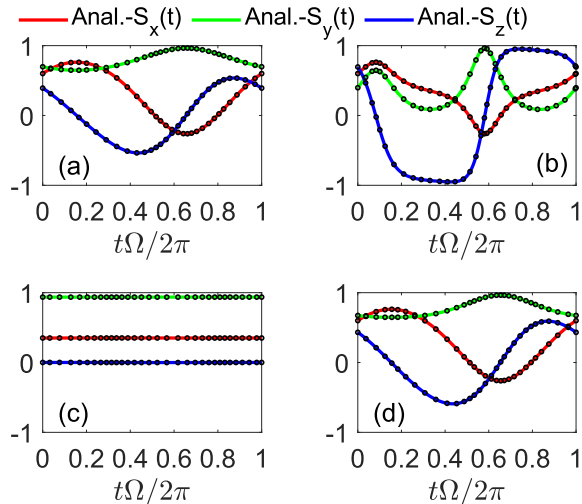


**Fig. 5:** (color online) Comparisons between the analytical solutions Eq. (50) and the numerical ones Eq. (4). The solid red, green and blue line corresponds to the  $S_x(t)$ ,  $S_y(t)$  and  $S_z(t)$ , respectively. While the black circles are the corresponding results obtained by numerically solving Eq. 4. For subplot (a-d), (a)  $g_1 = 4$  and  $g_2 = g_-(f_0) + \epsilon$ ; (b),  $g_1 = 4$  and  $g_2 = g_+(f_0) - \epsilon$ ; (c),  $g_1 = g_+(f_0) + \epsilon$  and  $g_2 = 1$ ; (d),  $g_1 = 4$  and  $g_2 = 1$ . Here  $f_0 = 1.6$  and  $\epsilon$  is an infinitesimal positive real number.

Fig. 6 demonstrates the typical dynamical phase diagram in terms of time-averaged order parameter  $\bar{S}_z = \int_0^T dt S_z(t)/T$  after quenching the nonlinear interactions  $(g_1, g_2)$  from the initial values  $(g_{1,i}, g_{2,i})$  ( $g_{1,i} > g_{2,i}$ ) to the final ones  $(g_{1,f}, g_{2,f})$ . Here we take  $g_{2,i} = -4$  as an example. The initial state is the ferromagnetic ground state, breaking a  $Z_2$  symmetry, with  $S_z(0) = \sqrt{1 - g_{2,i}^{-2}} > 0$  and  $S_y(0) = 0$  ( $\theta_0 = \arcsin(-1/g_{2,i})$  and  $\phi_0 = \pi$ ) when  $g_{1,i} > g_{2,i}$  and  $g_{2,i} \leq -1$ . It becomes clear that the phase diagram of DPT (marked by the white thick dashed lines in Fig. 6) is inconsistent with the one of its equilibrium counterpart (by the black thick dashed (second order)/solid (first order) lines in Fig. 6). In detail, when  $g_{1,f} \geq -1$ , the lower boundary of DPT  $g_{2,f}^-$  is obtained by  $f_0(g_{1,f}, g_{2,f}, \theta_0, \phi_0) = -1$ ,

$$g_{2,f}^- = \frac{-2g_{2,i}}{g_{2,i} - 1}. \quad (52)$$

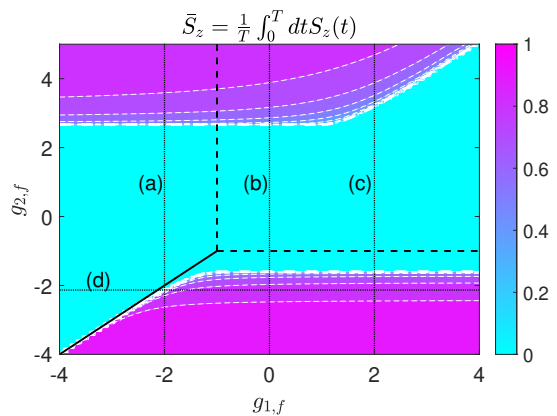


**Fig. 6:** (color online) Dynamical phase diagram of the generic LMG model in terms of time-averaged order parameter  $\bar{S}_z = \int_0^T dt S_z(t)/T$  in the thermodynamic limit when  $g_{2,i} = -4 < g_{1,i} \leq -1$ . The boundaries of DPT are marked as white thick dashed lines. As a comparison, we also depict the corresponding zero-temperature phase diagram of equilibrium system (black thick solid (first order) and dashed (second order) lines).

And when  $g_{1,f} \leq 1$  the upper boundary  $g_{2,f}^+$  is determined by  $f_0(g_{1,f}, g_{2,f}, \theta_0, \phi_0) = 1$ ,

$$g_{2,f}^+ = \frac{2g_{2,i}}{g_{2,i} + 1}. \quad (53)$$

While the lower boundary as  $g_{1,f} < -1$  and the upper one as  $g_{1,f} > 1$  is controlled by  $f_0(g_{1,f}, g_{2,f}, \theta_0, \phi_0) = \frac{1}{2}(g_{1,f} + 1/g_{1,f})$  and written in a unified formula,

$$\frac{g_{2,i}(g_{2,i} + g_{1,f}(g_{1,f}g_{2,i} - 2))}{g_{1,f}(g_{2,i}^2 - 1)} = \begin{cases} g_{2,f}^-, & g_{1,f} < -1 \\ g_{2,f}^+, & g_{1,f} > 1 \end{cases}. \quad (54)$$

In fact, these critical lines ( $g_{2,f}^\pm$ ) can be uniformly understood as the conditions under which the post-quenched energy  $f_0(g_{1,f}, g_{2,f}, \theta_0, \phi_0)$  intersects one of the saddle points, namely  $f_0 = \pm 1$  or  $f_0 = \frac{1}{2}(g_{1,f} + 1/g_{1,f})$ , as illustrated in Fig. 7 for a specific case of  $g_{1,f} = -2$  (labeled as (a) in Fig. 6). When  $g_{2,f} < g_{2,f}^-$ , the dynamics is largely determined by the global minimum  $f_0 = (g_{2,f} + 1/g_{2,f})$  and trapped in the northern hemisphere of Bloch sphere with finite time-averaged order

parameter  $\bar{S}_z$ , which is a reminiscent of mesoscopic self-trapping (MST) mode with oscillating phase. However, as  $g_{2,f} \rightarrow g_{2,f}^-$ , the classical trajectory gradually approaches to the one (marked as red solid line in Fig. 7) close to the saddle points  $f_0 = \frac{1}{2}(g_{1,f} + 1/g_{1,f})$  (marked as black solid circles in Fig. 7) and sharply jumps to the one with vanished  $\bar{S}_z$  (magenta solid line in Fig. 7) as  $g_{2,f}$  crossing the critical point  $g_{2,f}^-$ . Therefore, a DPT occurs at  $g_{2,f} = g_{2,f}^-$  and the  $Z_2$  symmetry restores again. Here it is worthy noting that the two saddle points (black solid circles) finally merge with each other at  $(\theta_0, \phi_0) = (\pi/2, \pi)$  as  $g_{1,f} \rightarrow 0$ . Furthermore as  $g_{2,f}^- < g_{2,f} \leq g_{2,f}^+$ , the dynamics holds this  $Z_2$  symmetry with  $\bar{S}_z = 0$  until its trajectory intersects the second saddle point  $(\theta_0, \phi_0) = (\pi/2, 0)$  ( $f_0 = 1$ ). Finally, another DPT occurs and breaks its corresponding  $Z_2$  symmetry again as  $g_{2,f}$  crossing  $g_{2,f}^+$  (exemplified by the solid green and blue lines in Fig. 7). However, these emerged MST modes are different from the ones when  $g_{2,f} < g_{2,f}^-$ , due to the nature of running phase.

In the thermodynamic limit, DPT is triggered and controlled by the classical saddle points of isoenergetic surface. Actually the time-averaged order parameter, i.e.,  $\bar{S}_z$ , displays a logarithmic singularity [32] around dynamical critical points (i.e.,  $g_{2,f}^\pm$ ), largely distinct from its equilibrium counterpart. Here we take four examples to demonstrate the evolution as varying the quenching parameter in Fig. 8. Especially, in the second scenario ((a,c,d) in Fig. 8), we observe that as  $g_{2,f}$  varies, the dynamical criticality of DPT exhibits similar behavior in terms of time-averaged order parameter  $\bar{S}_z$ , but distinct behavior in terms of  $\bar{S}_x$ , which requires further investigations.

At last, we briefly discuss the corresponding detection of DPTs in terms of BEC trapped in a toroidal trap where both scenarios of LMG model (Eq. 1) can be engineered in a realistic setup, following the Ref. [15]. To engineer the LMG model Eq. (1), two counter-propagating rotational modes of a homogeneous ring trap are initially populated while the remained modes are gaped away because of the large kinetic energy gap. And the interaction between the two Bosonic modes, imposed by the mechanism of an optical Feshbach resonance, varies along the azimuth angle, specifically,  $g(\phi, t) \propto g_0 + g_1 \cos(4q(\omega t + \phi))$ . Here

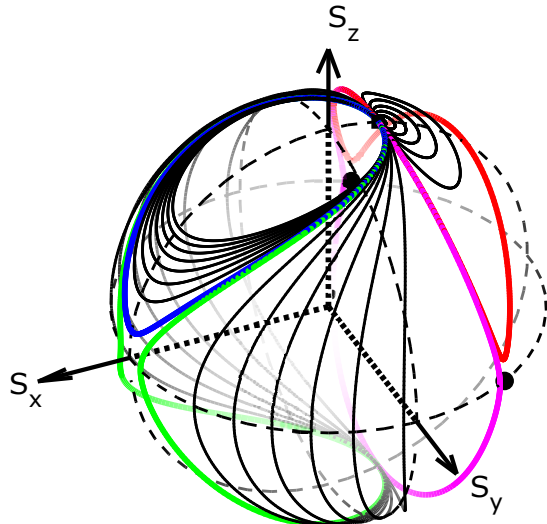


**Fig. 7:** (color online) Quench dynamics of Eq. (4) in the thermodynamic limit is depicted on Bloch sphere after a quench  $g_{2,f}$  as  $g_{1,f} = -2$  (labeled as (a) as the black thin dashed line in Fig. 6). Here four special trajectories are chosen to emphasize the two DPT transitions, the solid red, magenta, green and blue line represents the relevant classical trajectory with  $g_{2,f} = g_{2,f}^- - \epsilon$ ,  $g_{2,f}^- + \epsilon$ ,  $g_{2,f}^+ - \epsilon$  and  $g_{2,f}^+ + \epsilon$ , respectively. Here  $\epsilon$  is a positive infinitesimal constant.

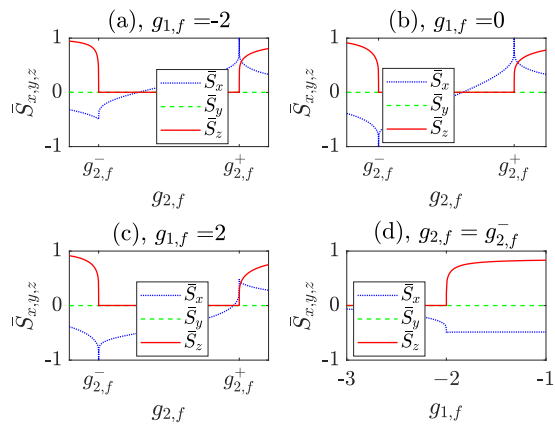


**Fig. 8:** (color online) DPT as quenching control parameters from i.e.,  $(g_{1,i}, g_{2,i} = -4)$  (take  $g_{1,i} > g_{2,i}$  to ensure the initial state is the ferromagnetic ground state) to the final parameters,  $(g_{1,f}, g_{2,f})$ . Here we choose  $g_{1,f} = -2$  (a), 0 (b), 2 (c) as varying  $g_{2,f}$ , and  $g_{2,f} = g_{2,f}^-$  (d) as varying  $g_{1,f}$  to demonstrate the evolution of time-averaged order parameters  $\bar{S}_{x,y,z}$ . Here  $\bar{S}_y$  is always zero.

$g_{0,1}$  represents the strength of static and modulated interaction, both of which can be finely tuned,  $q$  is an integer number,  $\omega$  is the modulation frequency. Then Eq. (1) is finally obtained under a spin rotation, i.e.,  $\hat{J}_x \rightarrow \hat{J}_y$ ,  $\hat{J}_y \rightarrow \hat{J}_z$  and  $\hat{J}_z \rightarrow \hat{J}_x$ , with the effective Hamiltonian  $\hat{H}_{\text{eff}} = 2q\omega\hat{J}_z + (\frac{\chi_+}{2} + \chi_0)\hat{J}_x^2 + (-\frac{\chi_+}{2} + \chi_0)\hat{J}_y^2$ , where  $\hat{J}_{x,y,z}$  shares the same definition as in the Section 1,  $\hat{a} \equiv \hat{a}_q e^{-iq\omega t}$  and  $\hat{b} \equiv \hat{a}_{-q} e^{iq\omega t}$ . Based on the advanced time-of-flight technique, the aforementioned DPTs can be well extracted by measuring its azimuth density  $n(\phi, t) = \langle \Psi_0 | \hat{\psi}^\dagger(\phi, t) \hat{\psi}(\phi, t) | \Psi_0 \rangle \propto 1 + S_y(t) \cos(2q\omega t + \phi) - S_z(t) \sin(2q\omega t + \phi)$  with  $\hat{\psi}(\phi, t) \propto \hat{a}_q e^{iq\phi} + \hat{a}_{-q} e^{-iq\phi}$ .

## 4 Conclusions

In this work, we have analytically obtained the exact classical dynamics of the generic LMG model in the thermodynamic limit by constructing an auxiliary function  $X(t) = a_1 S_y(t) + a_2 S_z(t)$ . This construction works because all the extrema of  $f_0$  depend solely on one nonlinear interaction, i.e., either on  $g_1$  or on  $g_2$ , as seen in Eq. (10). As a consequence, we conclude that the classical dynamics of generic LMG model also can be one-by-one mapped into, besides the usual Bloch sphere, the complex plane of one member of Jacobi elliptic functions. Based on the obtained analytical solutions Eq. (21)(30)(39)(50), we further give the dynamical phase diagram in terms of time-averaged order parameter after a quench of two nonlinear interactions ( $g_1, g_2$ ), and analytically discuss the properties of dynamical phase transitions triggered by the saddle points of isoenergetic surface. Particularly in the second scenario ( $g_{1,f} g_{2,f} \neq 0$ ), we observe that the dynamical criticality depends on the choice of time-averaged order parameter. Our results would be detected in a BECs trapped in a homogeneous toroidal trap. Our works is useful to estimate entanglement dynamics of this generic LMG model, and also investigate the corresponding dynamical phase transitions in presence of dissipation or decoherence [33] which is left as future work.

**Acknowledgments.** The author thanks Dr. Siqi Ren for stimulating discussions, and also thanks Prof. Chao Gao for helpful suggestions on organization and English grammar of our

manuscript. This work was supported by the starting fund of Zhejiang University of Technology.

**Data Availability Statement.** This manuscript has no associated data or the data will not be deposited. [Authors comment: The datasets generated and/or analyzed during the current study are available from the corresponding author on reasonable request.]

## Appendix A

The constructions of  $S_{x,y,z}(t)$  based on the solutions  $X(t)$  (Eq. (15)) hinges on the signs of  $g_1$  and  $g_2$ , therefore, four cases are listed below.

Case I: when  $g_1 > 0$  and  $g_2 < 0$ , set  $X_\pm = a_1 S_y \pm a_2 S_z$ , the solutions can be written down as

$$S_y = \frac{X_+ + X_-}{2a_1}, \quad S_z = \frac{X_+ - X_-}{2a_2}. \quad (\text{A1})$$

Case II: when  $g_1 < 0$  and  $g_2 > 0$ , set  $X_\pm = \pm a_1 S_y + a_2 S_z$ ,

$$S_y = \frac{X_+ - X_-}{2a_1}, \quad S_z = \frac{X_+ + X_-}{2a_2}. \quad (\text{A2})$$

Case III: when  $g_1 > g_2 > 0$  or  $g_1 < g_2 < 0$ ,

$$S_y = \frac{X + X^*}{2a_1}, \quad S_z = \frac{X - X^*}{2a_2}. \quad (\text{A3})$$

Case IV:  $0 < g_1 < g_2$  or  $g_2 < g_1 < 0$ ,

$$S_y = \frac{X - X^*}{2a_1}, \quad S_z = \frac{X + X^*}{2a_2}. \quad (\text{A4})$$

Finally,  $S_x(t)$  is obtained accordingly,

$$S_x = f_0 - \frac{1}{2}(g_1 S_y^2 + g_2 S_z^2) \quad (\text{A5})$$

## Appendix B

In this Appendix, we will present how to solve a equation [34] like,

$$(d_t X)^2 = P[X] = \sum_{j=0}^4 C_j X^j, \quad (\text{B6})$$

with real coefficients  $C_j$ .

Supposing that the four roots of  $P[X] = 0$ , i.e.,  $a, b, c$  and  $d$ , are already known,  $P[X]$  can be factorized as follow,

$$P[X] = S_1 S_2, \quad (\text{B7})$$

with

$$\begin{aligned} S_1 &= p_1(X - a)(X - b) = p_1 X^2 + 2q_1 X + r_1, \\ S_2 &= p_2(X - c)(X - d) = p_2 X^2 + 2q_2 X + r_2. \end{aligned} \quad (\text{B8})$$

Therefore,  $p_1 = 1$ , and  $p_2 = C_4$ ,

$$\begin{aligned} q_1 &= -\frac{p_1}{2}(a + b), \quad r_1 = p_1 ab, \\ q_2 &= -\frac{p_2}{2}(c + d), \quad r_2 = p_2 cd. \end{aligned} \quad (\text{B9})$$

Next, we look for a parameter  $\lambda$  such that

$$\begin{aligned} S_1 - \lambda S_2 &= (p_1 - \lambda p_2)X^2 + 2(q_1 - \lambda q_2)X + (r_1 - \lambda r_2) \tilde{\Delta} = (p_1 r_2 - p_2 r_1)^2 - 4(p_1 q_2 - p_2 q_1)(q_1 r_2 - q_2 r_1), \\ &= (p_1 - \lambda p_2)(X - \alpha)^2, \end{aligned} \quad (\text{B10}) \quad = (p_1 p_2)^2 (a - c)(b - c)(a - d)(b - d), \quad (\text{B17})$$

therefore, the discriminant of above quadratic polynomial with variable  $X$  must be zero,

$$(q_1 - \lambda q_2)^2 - (p_1 - \lambda p_2)(r_1 - \lambda r_2) = 0. \quad (\text{B11})$$

In general, Eq. (B11) would have two different roots, the another is labeled as  $\mu$ . While  $\alpha$  (the root of  $S_1 - \lambda S_2$ ) can be obtained by comparing the coefficient of  $X$  in both sides of Eq.(B10), as a result,

$$\lambda = \frac{\alpha p_1 + q_1}{\alpha p_2 + q_2}. \quad (\text{B12})$$

Substituting  $\lambda$  of Eq. (B11) with Eq. (B12), we obtain

$$\begin{aligned} (p_1 q_2 - p_2 q_1) \cdot ((p_1 q_2 - p_2 q_1) \alpha^2 \\ + (p_1 r_2 - p_2 r_1) \alpha + q_1 r_2 - q_2 r_1) = 0, \end{aligned} \quad (\text{B13})$$

with

$$\begin{aligned} p_1 q_2 - p_2 q_1 &= -\frac{p_1 p_2}{2}(c + d - a - b), \\ p_1 r_2 - p_2 r_1 &= p_1 p_2 (cd - ab), \\ q_1 r_2 - q_2 r_1 &= -\frac{p_1 p_2}{2}((a + b)cd - (c + d)ab). \end{aligned}$$

(B14)

Two cases have to be discussed. The first case is  $p_1 q_2 = p_2 q_1$ , which results from  $a + b = c + d$ .  $P[X]$  is written down as follow,

$$\begin{aligned} P[X] &= p_1 p_2 \cdot \\ &((X - \alpha)^2 + ab - \alpha^2)((X - \alpha)^2 + cd - \alpha^2), \end{aligned} \quad (\text{B15})$$

with  $\alpha = (a + b)/2$ . Therefore, Eq. (B6) becomes

$$\begin{aligned} (d_t X)^2 &= p_1 p_2 ((X - \alpha)^2 + ab - \alpha^2) \\ &\cdot ((X - \alpha)^2 + cd - \alpha^2). \end{aligned} \quad (\text{B16})$$

While the second case  $p_1 q_2 \neq p_2 q_1$  would be a little complex. The discriminant of Eq. (B13)  $\tilde{\Delta}$  can be simplified as follow,

which is a real and positive number, namely  $\tilde{\Delta} > 0$ , proven by dividing it into three cases: Case (1),  $\{a, b, c, d\} \in \mathcal{R}$ , and without loss of generality, we can choose  $a > b > c > d$ , therefore,  $\tilde{\Delta} > 0$ . Case (2), one pair root of  $P[X] = 0$  are complex numbers while the another are real ones, i.e.,  $c = d^*$  while  $\{a, b\} \in \mathcal{R}$ , then  $\tilde{\Delta} = (p_1 p_2)^2 |a - c|^2 \cdot |b - c^*|^2 > 0$ . Case (3), all roots of  $P[X] = 0$  are complexes, then  $\tilde{\Delta} = (p_1 p_2)^2 |a - c|^2 \cdot |a^* - c|^2 > 0$ .

Supposing that the two real roots of Eq. (B13) are labeled as  $\alpha$  and  $\beta$  ( $\alpha > \beta$  is assumed without loss of generality). When  $p_1 q_2 > p_2 q_1$ ,

$$\alpha = \frac{p_1 p_2 (ab - cd) + \sqrt{\tilde{\Delta}}}{p_1 p_2 (a + b - c - d)}, \quad (\text{B18})$$

$$\beta = \frac{p_1 p_2 (ab - cd) - \sqrt{\tilde{\Delta}}}{p_1 p_2 (a + b - c - d)}, \quad (\text{B19})$$

(B20)

otherwise

$$\alpha = \frac{p_1 p_2 (ab - cd) - \sqrt{\tilde{\Delta}}}{p_1 p_2 (a + b - c - d)}, \quad (\text{B21})$$

$$\beta = \frac{p_1 p_2 (ab - cd) + \sqrt{\tilde{\Delta}}}{p_1 p_2 (a + b - c - d)}. \quad (\text{B22})$$

(B23)

and consequently

$$\begin{aligned}\lambda &= \frac{p_1\alpha + q_1}{p_2\alpha + q_2}, \\ \mu &= \frac{p_1\beta + q_1}{p_2\beta + q_2}.\end{aligned}\quad (\text{B24})$$

Substituting the above equations into Eq. (B8), we finally get,

$$\begin{aligned}S_1 &= b_1(X - \alpha)^2 + c_1(X - \beta)^2, \\ S_2 &= b_2(X - \alpha)^2 + c_2(X - \beta)^2,\end{aligned}\quad (\text{B25})$$

with

$$\begin{aligned}b_1 &= \frac{p_1\beta + q_1}{\beta - \alpha}, \quad c_1 = \frac{p_1\alpha + q_1}{\alpha - \beta}, \\ b_2 &= \frac{p_2\beta + q_2}{\beta - \alpha}, \quad c_2 = \frac{p_2\alpha + q_2}{\alpha - \beta}.\end{aligned}\quad (\text{B26})$$

Making a transformation,  $Z = \frac{X - \alpha}{X - \beta}$ , we get

$$P[X] = \frac{(\alpha - \beta)^4}{(1 - Z)^4} (b_1 Z^2 + c_1)(b_2 Z^2 + c_2), \quad (\text{B27})$$

therefore,

$$(\partial_t Z)^2 = (\alpha - \beta)^2 (b_1 Z^2 + c_1)(b_2 Z^2 + c_2). \quad (\text{B28})$$

Up to a proportional constant, the differential equation of  $X$  (Eq. B16) or  $Z$  (Eq. B28) behaves identically with one member of family of Jacobi elliptic functions. Finally, the exact behavior of  $X$  would be obtained,

$$X = \frac{\beta Z - \alpha}{Z - 1}. \quad (\text{B29})$$

## Appendix C

In this appendix, we firstly demonstrate the oscillation frequency  $\Omega$  for arbitrary nonlinear couplings at a fixed  $f_0$  in thermodynamic limit (Fig. C1), which is helpful to uncover DPT of generic LMG model (Eq. (1)). Because  $f_0 = 1$  is a critical point as figured out in the main text, two cases are divided. The first case is  $0 \leq f_0 \leq 1$ . Basically, the oscillation frequency  $\Omega$  increases as far away from the dip zone around  $(g_1, g_2) = (0, 0)$

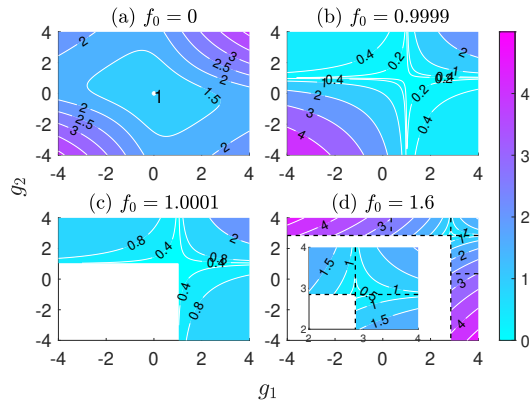


**Fig. C1:** (color online) Frequency  $\Omega$  versus  $g_1$  and  $g_2$  as varying  $f_0 = 0$ (a), 0.9999(b), 1.0001(c) and 1.6(d). A zoom-in around  $g_1 = g_2 = g_+(f_0)$  is shown in inset in Fig. C1(d).

when  $f_0 \approx 0$ . And the dip zone moves gradually to the regime around  $(g_1, g_2) = (1, 1)$  as  $f_0 \rightarrow 1$ , as depicted in Fig. (C1)(a,b), because  $f_0 = 1$  ( $(S_x, S_y, S_z) = (1, 0, 0)$ ) is a saddle point when  $(g_1 - 1)(g_2 - 1) < 0$ . The second case is  $f_0 \geq 1$ . Eq. (4) only exists when  $g_1 \geq g_+(f_0)$  and  $g_1 > g_2$ , or  $g_2 \geq g_+(f_0)$  and  $g_2 > g_1$ , demonstrated in Fig. (C1)(c,d). Around  $f_0 = 1$ , although  $\lim_{f_0 \rightarrow 1} \Omega = 0$ , a frequency discontinuity can be observed in Fig. (C1)(b,c) (see Eq. (36)) when  $(g_1 - 1)(g_2 - 1) < 0$ . Additionally,  $\Omega$  gets additional local minimum around  $g_2 = g_+(f_0)$ , which is proved to be exactly zero (Eq. (43)). This phenomena originate from a fact that the classical trajectories approach to another saddle point,  $f_0 = (g_2 + 1/g_2)/2$ . As a comparison,  $\Omega$  is finite and continuous around  $g_1 = g_+(f_0)$  or  $g_2 = g_-(f_0)$ .

Then we briefly discuss the landscape of  $f_0$  as varying  $\theta_0 \in (0, \pi)$  and  $\phi_0 \in (0, 2\pi)$ .

The first solution is  $\theta_0 = \pi/2$ ,  $\phi_0 = 0$ , then  $f_0 = 1$ , the Hessian matrix,

$$M = \begin{pmatrix} g_2 - 1 & 0 \\ 0 & g_1 - 1 \end{pmatrix}. \quad (\text{C30})$$

Therefore, this solution is a local minimum (maximum) when  $g_1 \geq 1$  and  $g_2 \geq 1$  ( $g_1 \leq 1$  and  $g_2 \leq 1$ ), which shows in Fig. (C2)(a,b,c,e,g). While in the rest regime ( $(g_1 - 1)(g_2 - 1) < 0$ ), it becomes a saddle point (Fig. (C2)(d,f)). The second solution  $\theta_0 = \pi/2$  and  $\phi_0 = \pi$ ,  $f_0 = -1$  and the



Hessian matrix,

$$M = \begin{pmatrix} g_2 + 1 & 0 \\ 0 & g_1 + 1 \end{pmatrix}, \quad (\text{C31})$$

a similar conclusion is given besides that the critical line becomes  $g_1 = -1$  and  $g_2 = -1$ .

The third solution includes four sub-solutions,  $\theta_0 = 0$  (or  $\pi$ ) and  $\phi_0 = \pi/2$  (or  $3\pi/2$ ), sharing the same energy  $f_0 = g_2/2$  and eigenvalues of its corresponding Hessian matrix,  $E_{\pm} = \frac{g_1 - g_2}{2} \pm \sqrt{\left(\frac{g_1 - g_2}{2}\right)^2 + 1}$ . Obviously,  $E_- < 0$  and  $E_+ > 0$  always hold for any value of  $g_1$  and  $g_2$ . Therefore, the four solution always are saddle points, see the pentagram symbols in Fig. (C2).

However, two additional solutions emerge when  $|g_1| \geq 1$  or  $|g_2| \geq 1$ . The fourth is  $\theta_0 = \pi/2$ ,  $\phi_0 = \arccos(1/g_1)$ ,  $f_0 = (g_1 + 1/g_1)/2$ , and the Hessian matrix,

$$M = \begin{pmatrix} g_2 - g_1 & 0 \\ 0 & \frac{1}{g_1} - g_1 \end{pmatrix}. \quad (\text{C32})$$

While the fifth is  $\phi_0 = 0$ ,  $\theta_0 = \arcsin(1/g_2)$  when  $g_2 > 1$ , and  $\phi_0 = \pi$ ,  $\theta_0 = \arcsin(-1/g_2)$  when  $g_2 < -1$ , the Hessian matrix,

$$M = \begin{pmatrix} \frac{1}{g_2} - g_2 & 0 \\ 0 & \frac{g_1 - g_2}{g_2^2} \end{pmatrix}. \quad (\text{C33})$$

Due to the time-reversal-like symmetry of Eq. (4), half  $g_1 - g_2$  plane is only needed to be discussed, i.e.,  $g_1 \geq g_2$ . Therefore, the properties of last two solution can be summarized as follow, the fourth one  $\theta_0 = \pi/2$  and  $\phi_0 = \arccos(1/g_1)$  is a local maximum (saddle point) when  $g_1 > 1$  ( $g_1 < -1$ ), which converges into the first solution at  $g_1 = \pm 1$ . While the fifth one  $\phi_0 = 0$  and  $\theta_0 = \arcsin(1/g_2)$  when  $g_2 \geq 1$  ( $\phi_0 = \pi$  and  $\theta_0 = \arcsin(-1/g_2)$  when  $g_2 \leq -1$ ) is a saddle point (local minimum), which converges into the second solution around  $g_2 = \pm 1$ , see Fig. (C2).

## References

- [1] Lipkin, H.J., Meshkov, N., Glick, A.J.: Validity of many-body approximation methods for a solvable model: (i). exact solutions and perturbation theory. *Nuclear Physics*

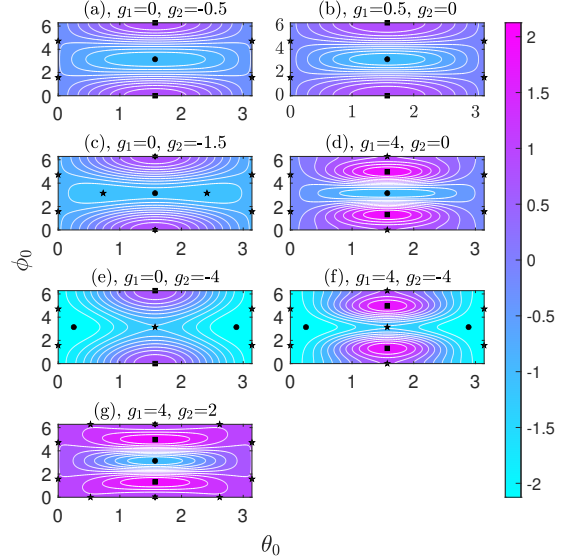


**Fig. C2:** (color online) Landscape of energy, Seven typical examples are chosen to demonstrate the frequency landscape as varying  $\theta_0$  and  $\phi_0$ . The global/local minimums, saddle points and global/local maximums are labeled by black circle/hexagon, pentagram and square/diamond symbols, respectively.

- 62**(2), 188–198 (1965) [https://doi.org/10.1016/0029-5582\(65\)90862-X](https://doi.org/10.1016/0029-5582(65)90862-X)
- [2] Meshkov, N., Glick, A.J., Lipkin, H.J.: Validity of many-body approximation methods for a solvable model: (ii). linearization procedures. *Nuclear Physics* **62**(2), 199–210 (1965) [https://doi.org/10.1016/0029-5582\(65\)90863-1](https://doi.org/10.1016/0029-5582(65)90863-1)
- [3] Glick, A.J., Lipkin, H.J., Meshkov, N.: Validity of many-body approximation methods for a solvable model: (iii). diagram summations. *Nuclear Physics* **62**(2), 211–224 (1965) [https://doi.org/10.1016/0029-5582\(65\)90864-3](https://doi.org/10.1016/0029-5582(65)90864-3)
- [4] Carrasco, J.A., Finkel, F., Gonzalez-Lopez, A., Rodriguez, M.A., Tempesta, P.: Generalized isotropic lipkin–meshkov–glick models: ground state entanglement and quantum entropies. *Journal of Statistical Mechanics: Theory and Experiment* **2016**(3), 033114 (2016) <https://doi.org/10.1088/1742-5468/>

- [5] Raghavan, S., Smerzi, A., Fantoni, S., Shenoy, S.R.: Coherent oscillations between two weakly coupled bose-einstein condensates: Josephson effects,  $\pi$  oscillations, and macroscopic quantum self-trapping. *Phys. Rev. A* **59**, 620–633 (1999) <https://doi.org/10.1103/PhysRevA.59.620>
- [6] Zibold, T., Nicklas, E., Gross, C., Oberthaler, M.K.: Classical bifurcation at the transition from rabi to josephson dynamics. *Phys. Rev. Lett.* **105**, 204101 (2010) <https://doi.org/10.1103/PhysRevLett.105.204101>
- [7] Baumann, K., Guerlin, C., Brennecke, F., Esslinger, T.: Dicke quantum phase transition with a superfluid gas in an optical cavity. *nature* **464**(7293), 1301–1306 (2010) <https://doi.org/10.1038/nature09009>
- [8] Muniz, J.A., Barberena, D., Lewis-Swan, R.J., Young, D.J., Cline, J.R.K., Rey, A.M., Thompson, J.K.: Exploring dynamical phase transitions with cold atoms in an optical cavity. *NATURE* **580**(7805), 602 (2020) <https://doi.org/10.1038/s41586-020-2224-x>
- [9] Chu, A., Will, J., Arlt, J., Klempt, C., Rey, A.M.: Simulation of  $xxz$  spin models using sideband transitions in trapped bosonic gases. *Phys. Rev. Lett.* **125**, 240504 (2020) <https://doi.org/10.1103/PhysRevLett.125.240504>
- [10] Xu, K., Sun, Z.-H., Liu, W., Zhang, Y.-R., Li, H., Dong, H., Ren, W., Zhang, P., Nori, F., Zheng, D., Fan, H., Wang, H.: Probing dynamical phase transitions with a superconducting quantum simulator. *Science Advances* **6**(25), 4935 (2020) <https://doi.org/10.1126/sciadv.aba4935>
- [11] Pezze, L., Smerzi, A., Oberthaler, M.K., Schmied, R., Treutlein, P.: Quantum metrology with nonclassical states of atomic ensembles. *Rev. Mod. Phys.* **90**, 035005 (2018) <https://doi.org/10.1103/RevModPhys.90.035005>
- [12] Morita, H., Ohnishi, H., Providencia, J., Nishiyama, S.: Exact solutions for the lmg model hamiltonian based on the bethe ansatz. *Nuclear Physics B* **737**(3), 337–350 (2006) <https://doi.org/10.1016/j.nuclphysb.2006.01.015>
- [13] Lerose, A., Marino, J., Zunkovic, B., Gambassi, A., Silva, A.: Chaotic dynamical ferromagnetic phase induced by nonequilibrium quantum fluctuations. *Phys. Rev. Lett.* **120**, 130603 (2018) <https://doi.org/10.1103/PhysRevLett.120.130603>
- [14] Viscondi, T.F., Furuya, K., De Oliveira, M.: Coherent state approach to the cross-collisional effects in the population dynamics of a two-mode bose-einstein condensate. *Annals of Physics* **324**(9), 1837–1846 (2009) <https://doi.org/10.1016/j.aop.2009.05.008>
- [15] Opatrny, T., Kolar, M., Das, K.K.: Spin squeezing by tensor twisting and lipkin-meshkov-glick dynamics in a toroidal bose-einstein condensate with spatially modulated nonlinearity. *Phys. Rev. A* **91**, 053612 (2015) <https://doi.org/10.1103/PhysRevA.91.053612>
- [16] Ma, J., Wang, X., Sun, C.P., Nori, F.: Quantum spin squeezing. *Physics Reports* **509**(2), 89–165 (2011) <https://doi.org/10.1016/j.physrep.2011.08.003>
- [17] Micheli, A., Jaksch, D., Cirac, J.I., Zoller, P.: Many-particle entanglement in two-component bose-einstein condensates. *Phys. Rev. A* **67**, 013607 (2003) <https://doi.org/10.1103/PhysRevA.67.013607>
- [18] Vidal, J., Palacios, G., Aslangul, C.: Entanglement dynamics in the lipkin-meshkov-glick model. *Phys. Rev. A* **70**, 062304 (2004) <https://doi.org/10.1103/PhysRevA.70.062304>
- [19] Lerose, A., Zunkovic, B., Marino, J., Gambassi, A., Silva, A.: Impact of nonequilibrium fluctuations on prethermal dynamical phase transitions in long-range interacting spin chains. *Phys. Rev. B* **99**, 045128 (2019) <https://doi.org/10.1103/PhysRevB.99.045128>

- [20] Marino, J., Eckstein, M., Foster, M.S., Rey, A.M.: Dynamical phase transitions in the collisionless pre-thermal states of isolated quantum systems: theory and experiments. *Reports on Progress in Physics* **85**(11), 116001 (2022) <https://doi.org/10.1088/1361-6633/ac906c>
- [21] Das, A., Sengupta, K., Sen, D., Chakrabarti, B.K.: Infinite-range ising ferromagnet in a time-dependent transverse magnetic field: Quench and ac dynamics near the quantum critical point. *Phys. Rev. B* **74**, 144423 (2006) <https://doi.org/10.1103/PhysRevB.74.144423>
- [22] Zunkovic, B., Silva, A., Fabrizio, M.: Dynamical phase transitions and loschmidt echo in the infinite-range xy model. *Philosophical Transactions of the Royal Society A: Mathematical, Physical and Engineering Sciences* **374**(2069), 20150160 (2016) <https://doi.org/10.1098/rsta.2015.0160>
- [23] Salas S, A.H., Altamirano, G.C., Martinez H, L.J.: Analytical solution to the generalized complex duffing equation. *The Scientific World Journal* **2022**, 2711466 (2022) <https://doi.org/10.1155/2022/2711466>
- [24] Castanos, O., Lopez-Pena, R., Hirsch, J.G., Lopez-Moreno, E.: Classical and quantum phase transitions in the lipkin-meshkov-glick model. *Phys. Rev. B* **74**, 104118 (2006) <https://doi.org/10.1103/PhysRevB.74.104118>
- [25] Ribeiro, P., Vidal, J., Mosseri, R.: Thermodynamical limit of the lipkin-meshkov-glick model. *Phys. Rev. Lett.* **99**, 050402 (2007) <https://doi.org/10.1103/PhysRevLett.99.050402>
- [26] Ribeiro, P., Vidal, J., Mosseri, R.: Exact spectrum of the lipkin-meshkov-glick model in the thermodynamic limit and finite-size corrections. *Phys. Rev. E* **78**, 021106 (2008) <https://doi.org/10.1103/PhysRevE.78.021106>
- [27] Krech, M.: Casimir forces in binary liquid mixtures. *Phys. Rev. E* **56**, 1642–1659 (1997) <https://doi.org/10.1103/PhysRevE.56.1642>
- [28] Armitage, J.V., Eberlein, W.F.: *Elliptic Functions*, pp. 1–24. Cambridge University Press, London (2006). <https://doi.org/10.1017/CBO9780511617867> . <https://doi.org/10.1017/CBO9780511617867>
- [29] Solinas, P., Ribeiro, P., Mosseri, R.: Dynamical properties across a quantum phase transition in the lipkin-meshkov-glick model. *Phys. Rev. A* **78**, 052329 (2008) <https://doi.org/10.1103/PhysRevA.78.052329>
- [30] Baksic, A., Ciuti, C.: Controlling discrete and continuous symmetries in superradiant phase transitions with circuit qed systems. *Phys. Rev. Lett.* **112**, 173601 (2014) <https://doi.org/10.1103/PhysRevLett.112.173601>
- [31] Soriente, M., Donner, T., Chitra, R., Zilberberg, O.: Dissipation-induced anomalous multicritical phenomena. *Phys. Rev. Lett.* **120**, 183603 (2018) <https://doi.org/10.1103/PhysRevLett.120.183603>
- [32] Li, B., Gao, C., Xianlong, G., Wang, P.: Critical behavior of the order parameter at the nonequilibrium phase transition of the ising model. *Journal of Physics: Condensed Matter* **31**(7), 075801 (2018) <https://doi.org/10.1088/1361-648X/aaf6cd>
- [33] Stitely, K.C., Giraldo, A., Krauskopf, B., Parkins, S.: Lasing and counter-lasing phase transitions in a cavity-qed system. *Phys. Rev. Res.* **4**, 023101 (2022) <https://doi.org/10.1103/PhysRevResearch.4.023101>
- [34] Wang, Z.X., Guo, D.R.: *Special Functions*, pp. 387–416. world scientific, Singapore (1989). <https://doi.org/10.1142/0653> . <https://doi.org/10.1142/0653>